Nanoscopic Management of Molecular Packing and Orientation of Small Molecules by a Combination of Linear and Branched Alkyl Side Chains

Minwoo Jung,[†,‡] Youngwoon Yoon,[†] Jae Hoon Park,[§] Wonsuk Cha,[∥] Ajeong Kim,[∥] Jinback Kang,[∥] Sanjeev Gautam,[⊥] Dongkyun Seo,[#] Jeong Ho Cho,[§] Hyunjung Kim,[∥] Jong Yong Choi,[†] Keun Hwa Chae,[⊥] Kyungwon Kwak,[#] Hae Jung Son,[†] Min Jae Ko,[†] Honggon Kim,[†] Doh-Kwon Lee,[†] Jin Young Kim,[†] Dong Hoon Choi,[‡] and BongSoo Kim[†,⊗,△,*]

[†]Photo-electronic Hybrids Research Center, Korea Institute of Science and Technology (KIST), Seoul 136-791, Republic of Korea, [‡]Department of Chemistry, Korea University, 1, Anam-dong 5-ga, Seongbuk-gu, Seoul 136-701, Republic of Korea, [§]SKKU Advanced Institute of Nanotechnology (SAINT) and Center for Human Interface Nano Technology (HINT), Department of Chemical Engineering, Sungkyunkwan University, Suwon 440-746, Republic of Korea, [∥]Department of Physics, Sogang University, Seoul 121-742, Republic of Korea, [⊥]Advanced Analysis Center, Korea Institute of Science and Technology (KIST), Seoul 136-791, Republic of Korea, [#]Department of Chemistry, Chung-Ang University, Seoul 156-756, Republic of Korea, [⊗]Green School, Korea University, 1, Anam-dong 5-ga, Seongbuk-gu, Seoul 136-701, Republic of Korea, and [△]Nanomaterials Science and Engineering, Korea University of Science & Technology, Daejeon 305-350, Republic of Korea

ABSTRACT We synthesized a series of acceptor−donor−acceptor-type small molecules (SIDPP-EE, SIDPP-EO, SIDPP-OE, and SIDPP-OO) consisting of a dithienosilole (SI) electron-donating moiety and two diketopyrrolopyrrole (DPP) electron-withdrawing moieties each bearing linear *n*-octyl (O) and/or branched 2-ethylhexyl (E) alkyl side chains. X-ray diffraction patterns revealed that SIDPP-EE and SIDPP-EO films were highly crystalline with pronounced edge-on orientation, whereas SIDPP-OE and SIDPP-OO films were less crystalline with a radial distribution of molecular orientations. Near-edge X-ray absorption fine structure spectroscopy disclosed an edge-on orientation with a molecular backbone tilt angle of ~22° for both SIDPP-EE and SIDPP-EO. Our analysis of the molecular packing and orientation indicated that the shorter 2-ethylhexyl groups on the SI core promote tight $\pi-\pi$ stacking of the molecular backbone, whereas *n*-octyl groups on the SI core hinder close $\pi-\pi$ stacking to some degree. Conversely, the longer linear *n*-octyl groups on the DPP arms facilitate close intermolecular packing *via* octyl−octyl interdigitation. Quantum mechanics/molecular mechanics molecular dynamics simulations determined the optimal three-dimensional positions of the flexible alkyl side chains of the SI and DPP units, which elucidates the structural cause of the molecular packing and orientation explicitly. The alkyl-chain-dependent molecular stacking significantly affected the electrical properties of the molecular films. The edge-on oriented molecules showed high hole mobilities in organic field-effect transistors, while the radially oriented molecules exhibited high photovoltaic properties in organic photovoltaic cells. These results demonstrate that appropriate positioning of alkyl side chains can modulate crystallinity and molecular orientation in SIDPP films, which ultimately have a profound impact on carrier transport and photovoltaic performance.

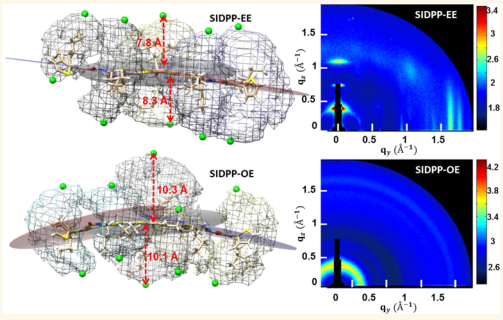

KEYWORDS: organic semiconductors · conjugated small molecules · molecular self-assembly · molecular orientation · hole mobility · power conversion efficiency · organic field-effect transistors · organic photovoltaic cells

Organic semiconductors are an important class of materials for optoelectronic applications, particularly with regard to organic field-effect transistors (OFETs) and organic photovoltaic cells (OPVs).[1−5] The design of new, promising organic semiconductors requires careful consideration of each part of the chemical structure for the target application. In OFETs, it is ideal that molecules in a channel have a well-ordered edge-on orientation with respect to the gate dielectric to facilitate hole or electron transport through intermolecular $\pi-\pi$ stacking.[6−8] Thus, edge-on oriented highly crystalline molecules exhibit high carrier mobility with low activation energy for carrier hopping. Moreover, energy level alignment between the molecular frontier orbital and the Fermi level (E_{Fermi}) of the contact metal is very

* Address correspondence to bongsoo@kist.re.kr.

Received for review February 25, 2014 and accepted May 26, 2014.

Published online May 26, 2014
10.1021/nn501133y

© 2014 American Chemical Society

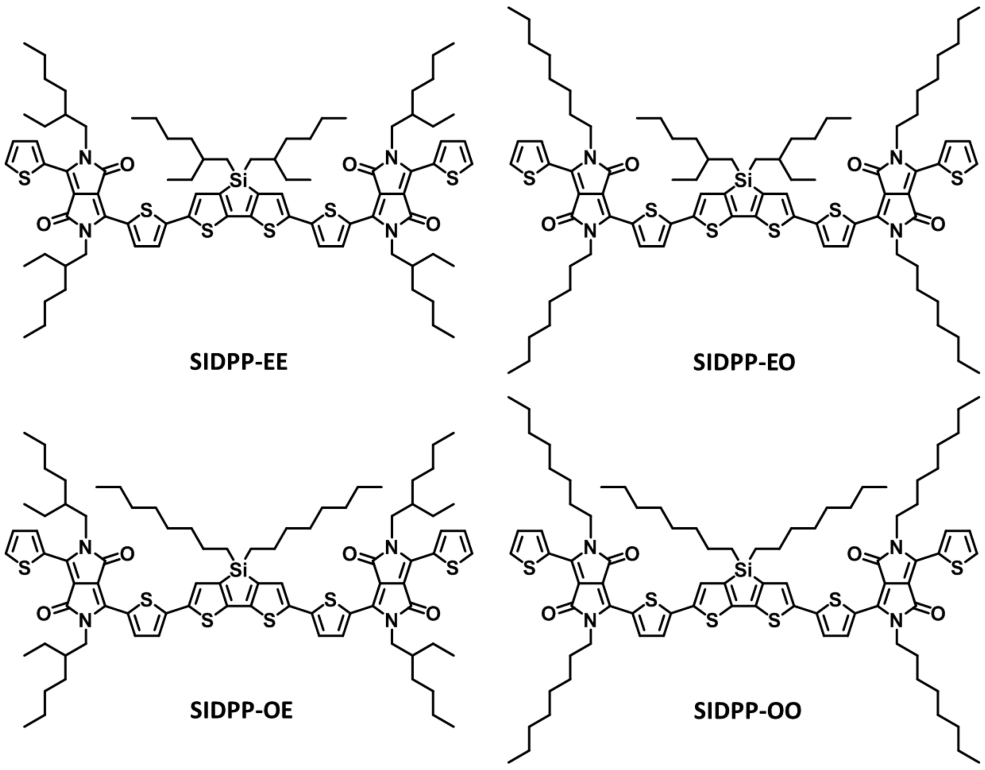

Figure 1. Molecular structure of SIDPP molecules.

important in determining the primary transport carrier type and the contact resistance.[9,10] For example, when the highest occupied molecular orbital (HOMO) level lies close to the E_{Fermi} of the contact metal (*e.g.*, Au), hole transport dominates and the smaller energy offset ($E_{Fermi} - E_{HOMO}$) gives a lower contact resistance.[11]

OPVs have stricter requirements because these devices involve a bulk-heterojunction-type photoactive layer consisting of electron-donor molecules and electron-acceptor molecules, typically fullerene derivatives.[12−16] The electron-donor molecules must possess a broad range of light absorption to capture solar energy and must possess optimal energy-level alignment with respect to the electron-acceptor molecules for efficient charge separation. As with OFETs, high carrier transport is essential; however, the carrier transport direction for OPVs is normal to the electrode. Thus, a face-on orientation of the aromatic molecular backbone would promote hole and electron transport for efficient charge collection.[17−20]

Recently, solution-processable low-band-gap small molecules have attracted considerable attention as OFETs and OPVs for several reasons: (1) synthesis and purification are relatively simple; (2) molecular energy levels can be tailored and closely predicted with advanced theoretical calculations; (3) batch-to-batch variation is minimal, yielding consistent electrical properties; and (4) promising molecules with high carrier mobilities and power conversion efficiencies (PCEs) have already been reported.[21,22] Molecules are typically composed of electron-donating (D) units and electron-withdrawing (A) units in a D-A-D or A-D-A pattern. While a variety of D and A moieties have been developed, the precise combination of these units dictates the electronic band gap, molecular energy levels, and intermolecular packing, as discussed previously.[16,23−27] To fully realize the intrinsic benefits of the chosen molecular units for high device performance, it is essential to systematically study the role of substituted alkyl side chains in determining electrical properties through their effect on molecular packing and molecular orientation.

In this work, we synthesized and characterized four alkyl side chain variants of the solution-processable small molecule 6,6′-((4,4-dialkyl-4*H*-silolo[3,2-*b*:4,5-*b*′]-dithiophene-2,6-diyl)bis(thiophene-5,2-diyl))bis(2,5-alkyl-3-(thiophen-2-yl)-2,5-dihydropyrrolo[3,4-*c*]pyrrole-1,4-dione) (SIDPP, Figure 1). The backbone of each molecule consists of dithienosilole (SI) and diketopyrrolopyrrole (DPP) moieties in a DPP-SI-DPP sequence. SI and DPP were chosen among the known D and A moieties for several reasons. SI moieties are a good electron-donating moiety, yielding strong intramolecular charge transfer characteristics and therefore low-energy optical transitions.[28,29] The four-coordinated silicon atom allows for the incorporation of two aliphatic side chains to modulate solubility characteristics, and the long Si−C bond promotes molecular linearity and facilitates molecular packing.[25,30−33] DPP moieties are photochemically stable and highly light-absorbing with strong electron-withdrawing properties.

Because they can be chemically bound to a number of electron-donating moieties to tailor electrical properties,[26] DPP units have frequently been incorporated in both polymer[34,35] and small-molecule OPVs.[23,24,27,36] Here the DPP-SI-DPP backboned molecules were found to be highly planar and promoted intramolecular π-delocalization and intermolecular stacking, lowering optical band gap and improving charge transport.

Branched 2-ethylhexyl (E) and linear *n*-octyl (O) alkyl substituents were investigated on the DPP-SI-DPP backbone, yielding four molecular variants, SIDPP-EE, SIDPP-EO, SIDPP-OE, and SIDPP-OO, where EE denotes 2-ethylhexyl substitutions on both SI and DPP moieties, EO denotes 2-ethylhexyl substitutions on the SI moiety and *n*-octyl substitutions on the DPP moieties, and so on. All alkyl side chains endowed the DPP-SI-DPP backbone with solubility in organic solvent, while their effect on crystallinity and molecular orientation differed significantly in cast films. X-ray diffraction patterns indicated that the SIDPP-EE and SIDPP-EO variants adopt a highly crystalline structure with a predominantly edge-on orientation, whereas the SIDPP-OE and SIDPP-OO films are less crystalline with a radial distribution of molecular orientations. Collective results of film characterization was well explained by calculation of molecular geometries; that is, the shorter 2-ethylhexyl groups on the SI core facilitate well-matched molecular packing, whereas the slightly longer *n*-octyl groups on the SI core prevent close molecular packing, yielding molecular disorder in the resulting films. The impact of molecular packing and orientation was examined by fabricating OFET and OPV devices. In OFET measurements high hole mobilities were observed in the highly crystalline edge-on oriented SIDPP-EE and SIDPP-EO molecules, while the highest PCE was observed by SIDPP-OE, which shows significant face-on molecular packing. *This work demonstrates that the position and branching of the alkyl side chains dramatically alter carrier mobility and photovoltaic performance through the control of molecular orientation and packing.*

RESULTS/DISCUSSION

Synthesis and Characterization. Scheme S1 shows the synthetic route and molecular structure of SIDPP-EE, SIDPP-EO, SIDPP-OE, and SIDPP-OO. Intermediate products **4**, **6**, and **8** were synthesized by reported literature procedures.[27,37] Final products were synthesized by Stille cross-coupling.[16,38] The SIDPP-EE, SIDPP-EO, and SIDPP-OE molecules were highly soluble in common organic solvents, including dichloromethane, chloroform, tetrahydrofuran, *N*,*N*-dimethylformamide, and toluene, whereas the SIDPP-OO bearing *n*-octyl side chains was less soluble.

Thermal Properties. Thermal properties of the SIDPP molecules were measured by differential scanning calorimetry (DSC) to determine crystallization temperatures (T_c) and melting temperatures (T_m) (Figure 2). DSC thermograms indicated that a combination of linear and branched alkyl side chains dramatically influences the thermal properties for a given molecular backbone. All molecules containing linear *n*-octyl groups underwent clear melting transitions on heating and crystallization transitions on cooling. Molecules bearing linear *n*-octyl side chains on the DPP moiety showed considerably increased melting temperatures as compared to molecules bearing 2-ethylhexyl groups. The large difference in T_m between SIDPP-OO with all linear side chains (T_m = 232.5 °C) and SIDPP-EE with all branched side chains (T_m = 174.8 °C) suggests that linear alkyl side chains on the DPP units promote a stronger intermolecular interaction when compared to branched alkyl side chains.[39,40] Interestingly, SIDPP-EE, functionalized with branched alkyl side chains, exhibits a cold crystallization at a lower temperature (110.6 °C) and a broad (or dual) melting transition with no crystallization on the cooling stage. This observation may indicate the existence of two $\pi-\pi$ stacking distances, which is supported by X-ray diffraction patterns (details were explained later). SIDPP-EE was also the most temperature-responsive of the series, resulting in a dramatic change in both crystallinity and hole mobility (see below). SIDPP-OE has the lowest T_m of 167.4 °C, indicating a lower cohesive energy. This can be attributed to (i) less favorable $\pi-\pi$ stacking caused by molecular crowding of the *n*-octyl groups on the SI core as compared to the 2-ethylhexyl groups and (ii) a weaker interaction between the 2-ethylhexyl groups on the DPP moiety observed by X-ray diffraction. The DSC findings indicate that the structure and position of the alkyl side chains are integral to intermolecular forces between SIDPP backbone molecules, thereby modulating T_m and T_c.[41−44]

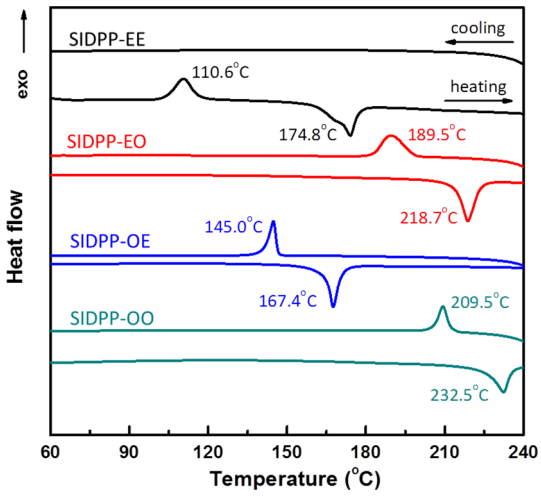

Figure 2. DSC thermograms of SIDPP molecules during first cooling and second heating scans (heating rate: 10 °C/min).

Optical and Electrochemical Properties. The optical properties of the SIDPP molecules were characterized by

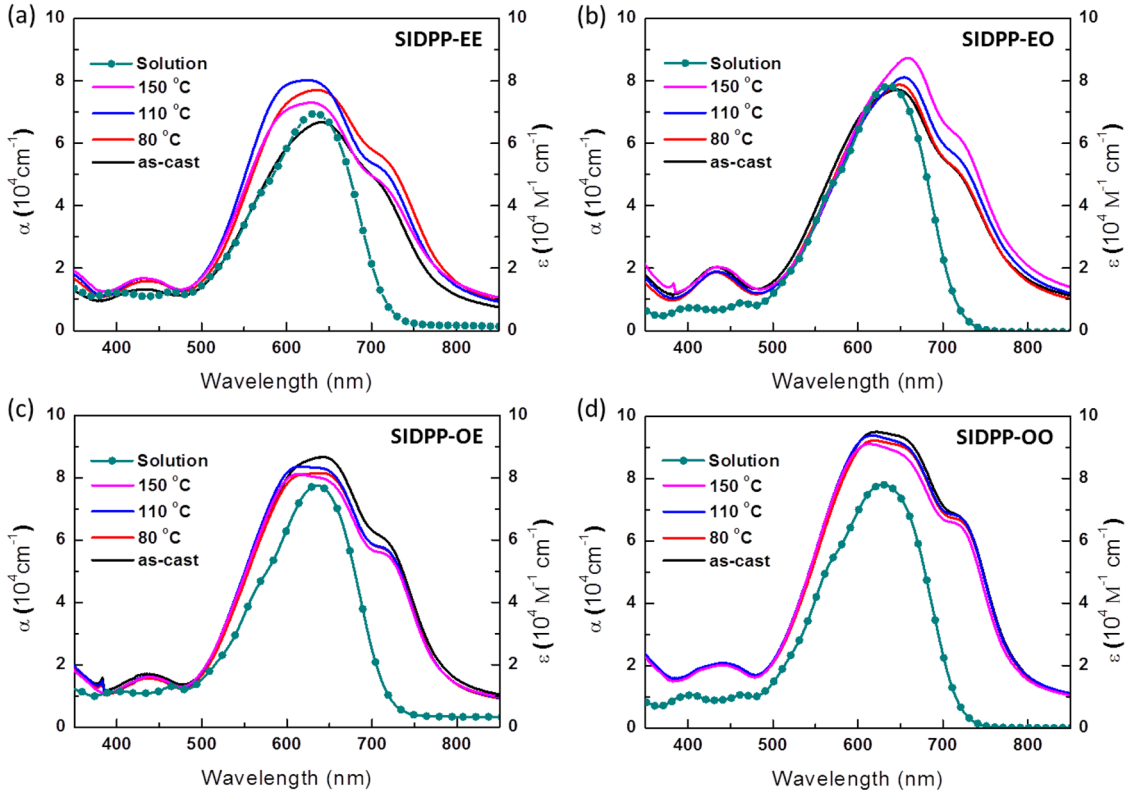

Figure 3. UV−visible absorption spectra of (a) SIDPP-EE, (b) SIDPP-EO, (c) SIDPP-OE, and (d) SIDPP-OO in solution phase (chloroform) and cast as a thin film. The thin films were annealed at room temperature (as-cast) and 80, 110, and 150 °C for 10 min.

TABLE 1. Optical and Electrochemical Properties of the SIDPP Molecules

	UV−visible absorption					cyclic voltammetry				
	solution		110 °C annealed film			as-cast film				
molecule	λ_{max} (nm)	λ_{onset} (nm)	λ_{max} (nm)	λ_{onset} (nm)	E_g^{opt} (eV)	E_{onset}^{ox} (V)[a]	HOMO (eV)[b]	E_{onset}^{red} (V)[c]	LUMO (eV)[d]	E_g^{EC} (eV)[e]
SIDPP-EE	630	716	620	780	1.59	0.29	−5.09	−1.54	−3.26	1.83
SIDPP-EO	636	718	650	791	1.57	0.24	−5.04	−1.57	−3.23	1.81
SIDPP-OE	635	716	618	781	1.59	0.26	−5.06	−1.63	−3.17	1.89
SIDPP-OO	630	719	613	785	1.58	0.29	−5.09	−1.62	−3.18	1.91

[a] The electrochemical oxidation onset potential in films with respect to the ferrocene/ferrocene$^+$. [b] HOMO is calculated by $-(E_{onset}^{ox} + 4.8$ eV). [c] The electrochemical reduction onset potential in films with respect to the ferrocene/ferrocenium. [d] HOMO is calculated by $-(E_{onset}^{ox} + 4.8$ eV). [e] Electrochemical band gap, i.e., LUMO−HOMO.

UV−visible absorption spectroscopy. Figure 3 shows UV−visible absorption spectra of each molecule in solution phase (chloroform) and cast as a thin film. Table 1 summarizes the resulting optical properties. In the solution state, UV−visible absorption features were nearly independent of the alkyl side chains for all SIDPP variants, and molecular extinction coefficients were high (6.8×10^4 to 8.0×10^4 M^{-1} cm^{-1}). In the solid state, the molecular films had high extinction coefficients (8.0×10^4 to 9.4×10^4 M^{-1} cm^{-1}) and showed red shifting of the absorption edge by approximately 60−70 nm with a peak at ~720 nm, a typical signature for J-aggregate formation.[27,45−47] Comparing the absorption maxima of the molecules indicated that SIDPP-EO had the largest red shift on going from solution phase to an annealed cast film. This suggests that the SIDPP-EO intermolecular interaction is quite intimate with less steric hindrance between the molecules by positioning 2-ethylhexyl groups at the SI core and *n*-octyl groups on the DPP side arms, as supported by X-ray diffraction patterns, which indicate tight $\pi-\pi$ stacking with a distance of 3.63 Å and interdigitation between *n*-octyl chains. It should be noted that the UV−visible absorption spectra of all the SIDPP molecules except SIDPP-EO exhibited blue shifting at around 600 nm in the cast films as well, indicating partial H-aggregate formation in addition to the formation of J-aggregates.[47−51] Thermal annealing induced more pronounced H-aggregate formation, and annealing the temperature-sensitive SIDPP-EE yielded

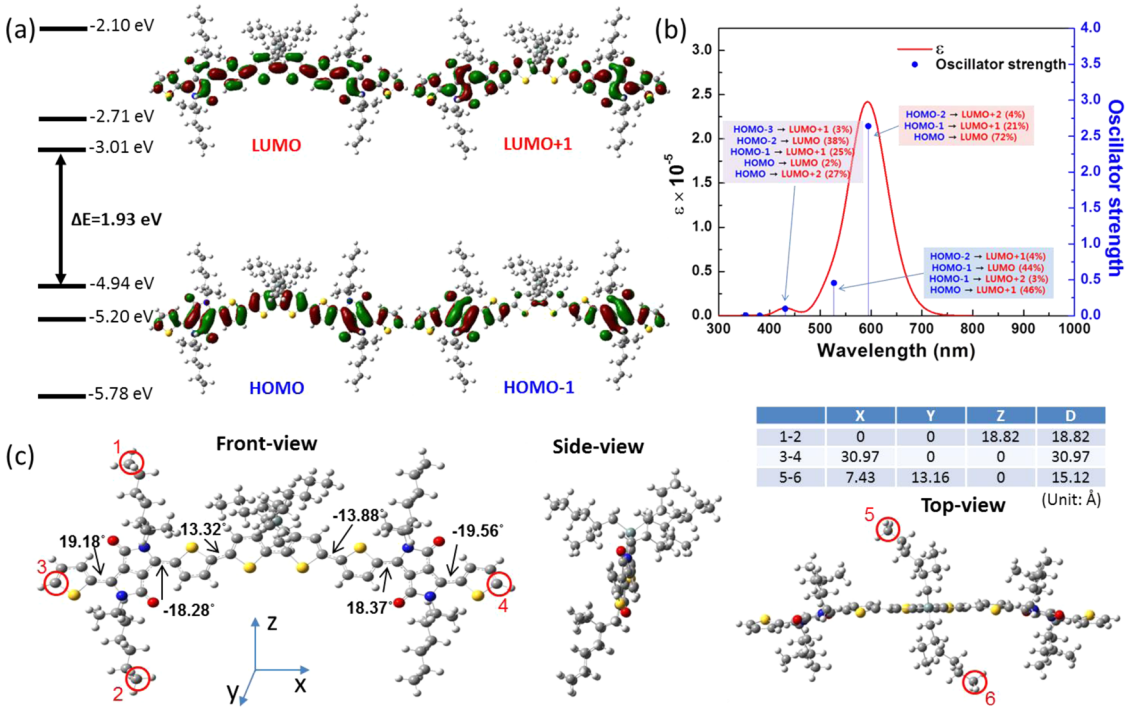

	X	Y	Z	D
1-2	0	0	18.82	18.82
3-4	30.97	0	0	30.97
5-6	7.43	13.16	0	15.12

Figure 4. (a) Energy levels (left) and frontier molecular orbitals of SIDPP-EE (right). (b) Absorption spectrum of SIDPP-EE (red), which is based on the TD-DFT (B3LYP) calculations of the electronic transition energy and oscillator strength (blue). (c) Energy minimum molecular geometry of SIDPP-EE with dihedral angles with a table summarizing numbered carbon-to-carbon interdistances.

a drastic change of absorption characteristics. Optical band gaps were determined from the 110 °C-annealed SIDPP molecular films and were estimated to be ~785 nm (1.58 eV) from the absorption edges.

Quantum mechanical calculations using density functional theory (DFT) and time-dependent DFT (TD-DFT) were employed to further examine the electronic structure, electronic transitions, and molecular geometries of the SIDPP molecular series. Details of the calculation can be found in the Supporting Information. The energy levels of frontier orbitals, electronic transition, and geometry of the SIDPP molecules were found to be nearly independent of alkyl side chain structure. Representative data and molecular models are presented for SIDPP-EE in Figure 4, and other molecular data sets can be found in Figures S1−S3. The HOMO and LUMO surface plots of SIDPP-EE display orbital delocalization throughout the molecular backbone with no contribution from alkyl side chain orbitals, as expected. This is consistent with the observed independence of frontier orbital energies on the alkyl side chains. Energy minimum geometries yield single-bond dihedral angles of less than 20° along the molecular backbone. Low dihedral angles ensure backbone planarity and effective overlap of π-orbitals.[52] The TD-DFT predictions agreed well with UV−visible spectral features of the SIDPP molecules. By comparing UV−visible absorption spectra to the TD-DFT calculations it becomes apparent that the HOMO−2 to LUMO, HOMO−1 to LUMO+1, and HOMO to LUMO+2 transitions are responsible for the absorption maximum at around 430 nm, while the HOMO to LUMO transition, which shows high oscillator strength, is responsible for the absorption maximum around 630 nm.

The electrochemical properties of the SIDPP molecules were examined by cyclic voltammetry (CV, Figure S4). Frontier molecular energy levels were determined from the onsets of the oxidation and reduction curves, and the HOMO and LUMO levels were located around −5.07 and −3.21 eV, respectively, for all SIDPP molecules. Thus, their electrochemical band gaps were ~1.86 eV. Note that high-lying HOMO levels imply that SIDPP molecules would be p-type in OFET devices,[9,11] and high-lying LUMO levels ensure efficient exciton splitting at the interface between SIDPP molecules and phenyl-C61-butyric acid methyl ester molecules (PCBM) in OPV devices.[13,14]

X-ray Diffraction. The microstructure and morphology of the SIDPP molecular films were assessed by X-ray diffraction (XRD) and grazing incidence X-ray diffraction (GIXD).[25,53−56] Figure 5 displays XRD spectra of SIDPP-EE and SIDPP-EO films as a function of annealing at room temperature (as-cast) and 80, 110, and 150 °C (XRD spectra of SIDPP-OE and SIDPP-OO films are shown in Figure S5). The as-cast films for all SIDPP molecules except SIDPP-EO displayed no diffraction peaks. Upon annealing, SIDPP-EE and SIDPP-EO films become highly crystalline, and SIDPP-EE, in particular, shows strong crystalline (100), (200), and (300) diffraction peaks. Note that single crystals could not be

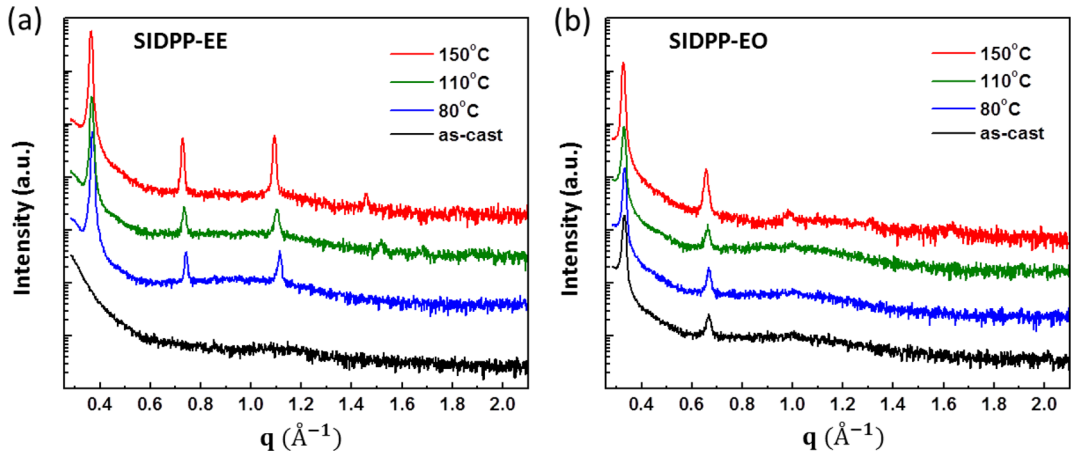

Figure 5. XRD patterns of (a) SIDPP-EE and (b) SIDPP-EO thin films as a function of annealing temperature.

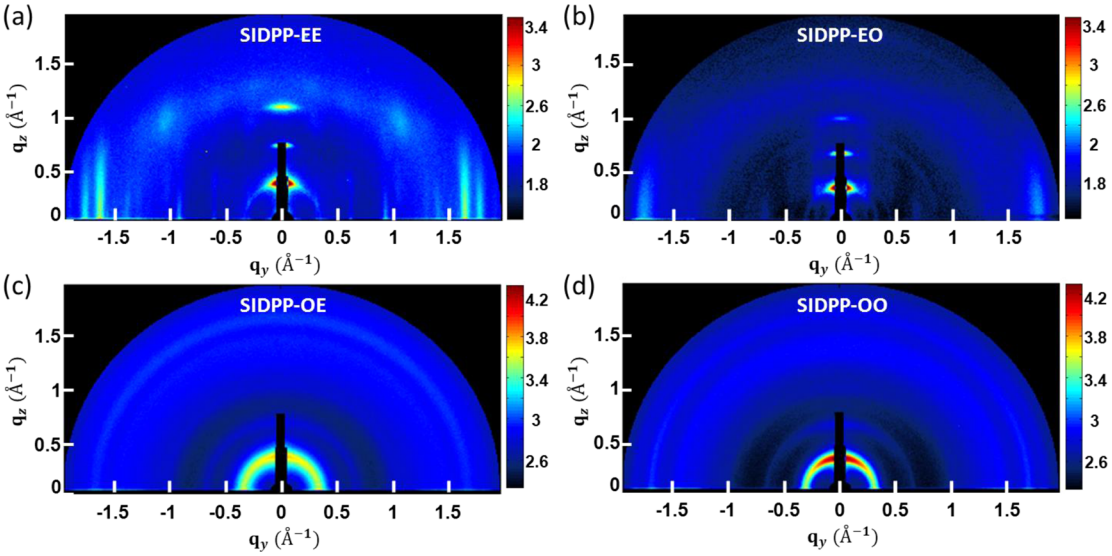

Figure 6. GIXD images of 110 °C-annealed (a) SIDPP-EE, (b) SIDPP-EO, (c) SIDPP-OE, and (d) SIDPP-OO thin films.

obtained; hence, conventional peak assignments were adopted for conjugated polymer peak assignments, as previously reported.[25,57,58] With increasing annealing temperature, both crystallinity and d_{h00} spacing increased gradually from q = 0.371 Å^{-1} (d = 16.9 Å) at 80 °C to q = 0.369 Å^{-1} (d = 17.0 Å) at 110 °C, and to q = 0.366 Å^{-1} (d = 17.2 Å) at 150 °C. The crystalline domain size also increased gradually from 48.7 nm at 80 °C to 50.3 nm at 150 °C, as calculated using the Scherrer equation: $D = 0.9\lambda/(\beta \cos \theta)$, where λ is the X-ray wavelength, β is the full width at half-maximum in radians (2θ), and θ is the scattering angle.[41] In SIDPP-EO films, the crystalline domain size increased similarly from 42.2 nm at room temperature to 46.7 nm at 150 °C.

Considering that the d_{h00} spacing (17.0 Å) at 110 °C is very close to the theoretical molecular width (18.82 Å) (assuming that the alkyl side chains are fully elongated), we conjecture that the molecular backbone is parallel to the substrate and that the alkyl side chains are oriented upward and downward as illustrated for SIDPP-EE in the side view of Figure 4c. This molecular orientation is supported by the GIXD and near-edge X-ray absorption fine structure (NEXAFS) data presented below. After annealing, the d_{h00} spacing of SIDPP-EE films increased, indicating increasing crystallinity and an edge-on orientation (Figures 5a, 6a, and S6a). Similarly, SIDPP-EO showed increasing intensity and therefore crystallinity for (100) and (200) peaks at higher annealing temperatures. However, these peak positions were independent of annealing temperature with q = 0.331 Å^{-1} (d_{h00} = 19.0 Å). This indicates that the as-cast SIDPP-EO films are highly crystalline, inherent to the molecules with high cohesive energy.

Further insight into molecular packing and orientation in the SIDPP molecular films was obtained from GIXD experiments. Figures 6 and S6 show GIXD images of 110 °C-annealed and as-cast SIDPP molecular films, respectively. The 110 °C-annealed SIDPP-EE and

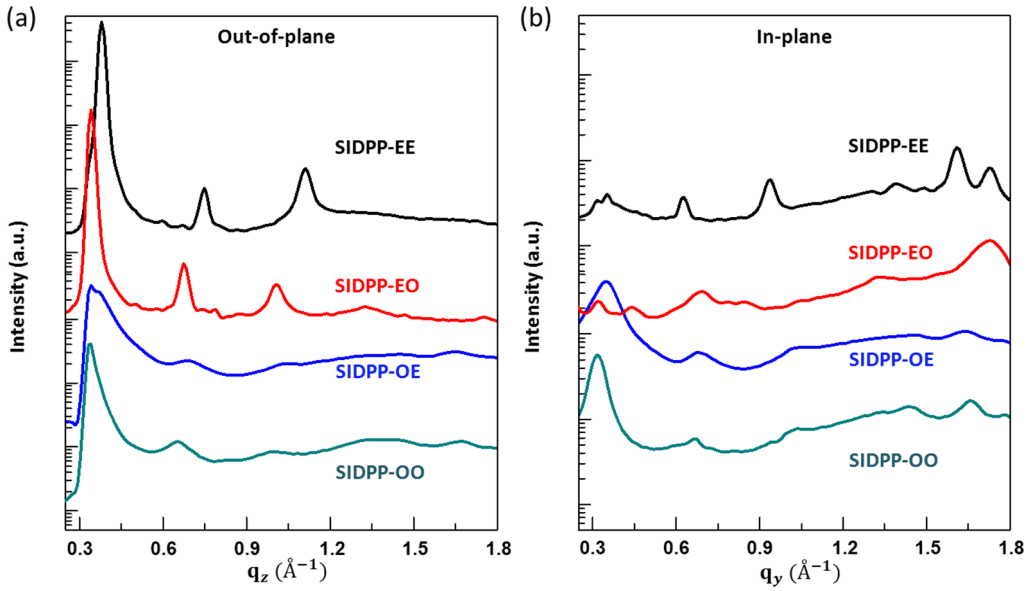

Figure 7. (a and b) Line-cut profiles in the out-of-plane (q_z) and in-plane (q_y) directions, respectively, in the GIXD images of 110 °C-annealed SIDPP molecular films.

SIDPP-EO films exhibited strong (100) peaks with high-order peaks in the out-of-plane (q_z) direction (Figure 6a,b), consistent with XRD results. Additional peaks including a (010) signal in the in-plane (q_y) direction were observed by increasing the intensity of the incident X-ray beam. Interestingly, the 110 °C-annealed SIDPP-EE films featured two (010) peaks at q = 1.618 Å^{-1} (d = 3.88 Å) and q = 1.725 Å^{-1} (d = 3.62 Å), both of which correspond to intermolecular $\pi-\pi$ distances. There are two possible explanations for the observed peaks. First, the (010) peaks may occur from both H-aggregates (lower q value) and J-aggregates (higher q value) present in the SIDPP-EE films. This is supported by (1) the UV−visible spectra, indicating H- and J-aggregate formation, which would have different molecular packing phases, (2) T_m peak broadening and shoulder formation, and (3) the higher q value being nearly identical to the (010) peak found at q = 1.733 Å^{-1} (d = 3.63 Å) in SIDPP-EO films, which forms predominantly J-aggregates. The second explanation is that the two peaks may correspond to two intermolecular $\pi-\pi$ distances between different aromatic rings in the molecular backbone. Very short $\pi-\pi$ distances close to the observed higher q value have been reported for di(ethylhexyl) SI moieties.[33,57] A clear understanding will require further experimental and theoretical work in molecular film states.

Use of a high-intensity X-ray beam disclosed features in the SIDPP-OE and SIDPP-OO films (Figure 6c,d). GIXD images revealed a radial distribution of the (100) diffraction peak and weak (010) peaks. Out-of-plane peaks were observed at q = 0.352 Å^{-1} (d = 17.9 Å) and q = 0.333 Å^{-1} (d = 18.9 Å), and intermolecular $\pi-\pi$ stacking peaks were observed at q = 1.636 Å^{-1} (d = 3.84 Å) and q = 1.654 Å^{-1} (d = 3.80 Å) for SIDPP-OE and SIDPP-OO films, respectively. The slightly longer $\pi-\pi$ stacking distances in these molecules than those in the SIDPP-EE and SIDPP-EO films indicate that intermolecular packing would be less favored in molecules with *n*-octyl attached to the SI core as opposed to 2-ethylhexyl substituents.

Line-cut profiles in the q_z and q_y directions indicate dramatic directional dependence in the intensities of the (100) and (010) peaks (Figure 7). SIDPP-EE and SIDPP-EO films show high contrast between (100) peak intensities in both directions, whereas SIDPP-OE and SIDPP-OO films display slightly higher (100) peak intensities in the q_z direction than in the q_y direction. The ratio of out-of-plane intensity (I_{oop}) to in-pane intensity (I_{ip}) of (100) peaks was estimated to be 1230, 3022, 2.5, and 7.5 for SIDPP-EE, SIDPP-EO, SIDPP-OE, and SIDPP-OO, respectively. These values indicate that the SIDPP-EE and SIDPP-EO molecules predominantly adopt an edge-on orientation, as illustrated in Figure 8a; SIDPP-OE and SIDPP-OO molecules also prefer an edge-on orientation, though they are mainly radially oriented, as shown in Figure 8c.

NEXAFS Spectroscopy. NEXAFS spectroscopy was used to confirm the orientation of the SIDPP backbone in thin films. NEXAFS spectroscopy is an element-specific, bond-sensitive technique that measures resonant excitations from carbon 1s core states to antibonding molecular orbitals such as π^* and σ^*. In total electron yield mode, the probing depth is approximately 6 nm,[59] thereby examining molecular orientations in both surface and bulk of films. NEXAFS peak intensity is proportional to the degree of overlap between the direction of an incident electric field and the molecule's orbital resonance excitation vector, *i.e.*, transition dipole moment (TDM). Figure S7 shows a schematic

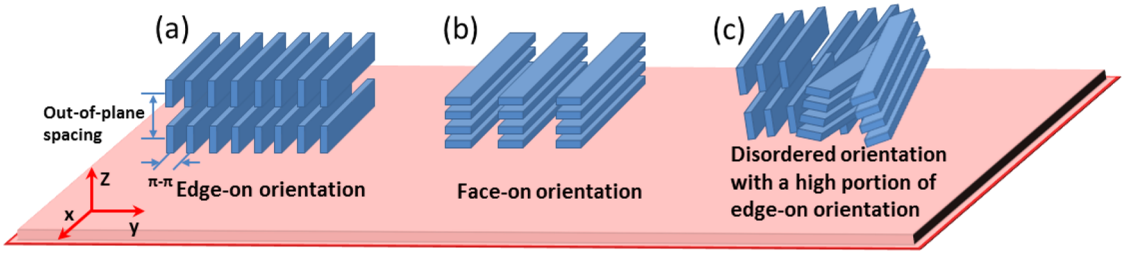

Figure 8. Schematic illustration of molecular orientation with respect to the substrate: (a) edge-on orientation, (b) face-on orientation, and (c) disordered orientation with a high portion of edge-on orientation.

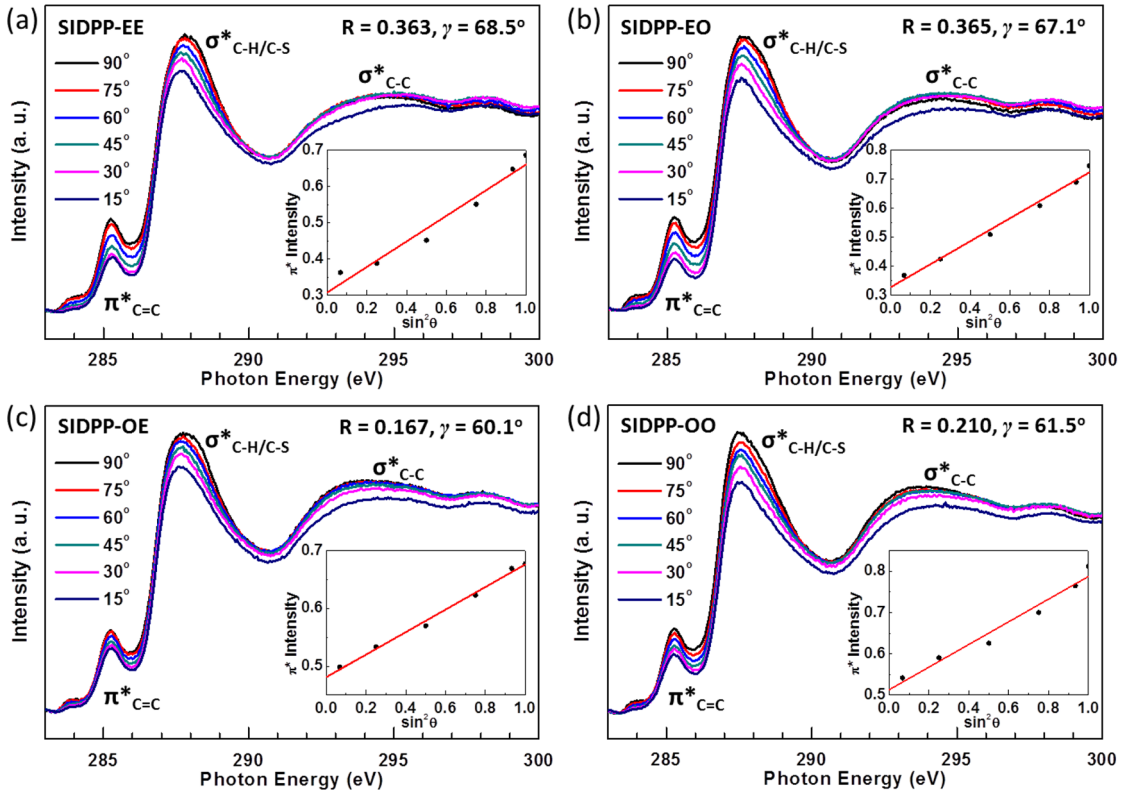

Figure 9. Carbon K-edge NEXAFS spectra for 110 °C-annealed (a) SIDPP-EE, (b) SIDPP-EO, (c) SIDPP-OE, and SIDPP-OO films with the incident angles and peak assignments. Insets depict the linear fit of the intensities of carbon−carbon 1s → π^* resonant excitation peaks.

illustration of the NEXFAS technique detailing the incident electric field vector (*E*), dichroic ratio (*R*), tilt angle (γ) of the TDM for the carbon−carbon 1s → π^* resonant excitation of the π-conjugated molecular backbone, and tilt angle (α) of the molecular backbone. The average orientation of the π-conjugated molecular backbone in thin films can be determined by the angle dependence of the excitation intensity.[55,60−62] SIDPP molecules are quite planar, so analysis of the lowest energy peaks arising from the 1s → π^* transition of π-conjugated molecular backbone carbon atoms was used to determine the molecular orientation. Since the peaks associated with carbon 1s → σ^* are superimposed, this technique was not used to determine the orientation of the alkyl side chains.

Figure 9 shows the NEXAFS spectra of the SIDPP molecules. The lowest energy NEXAFS peak at 285.3 eV corresponds to the carbon−carbon 1s → π^* resonant excitation of the carbon double bonds in the molecular backbone. The peak at 287.7 eV corresponds to both carbon−hydrogen 1s → σ^* and carbon−sulfur 1s → σ^* resonant excitations, and the peaks above 291 eV correspond to carbon−carbon 1s → σ^* resonant excitations.[55,60] The intensities of the carbon−carbon 1s → π^* peak at 285.3 eV in the SIDPP-EE and SIDPP-EO films increase significantly with increasing incident angles, while those in the SIDPP-OE and SIDPP-OO films increase with a lower slope. *R*, γ, and α values were calculated from the NEXAFS data as follows: (1) The intensities at $\theta = 90°$, *I*(90), and $\theta = 0°$, *I*(0), were estimated (Figure 9 insets) and used to calculate the *R* values of SIDPP-EE, SIDPP-EO, SIDPP-OE, and SIDPP-OO, which were found to be 0.363, 0.365, 0.167, and 0.210, respectively. (2) γ values of 68.5°, 67.1°, 60.1°,

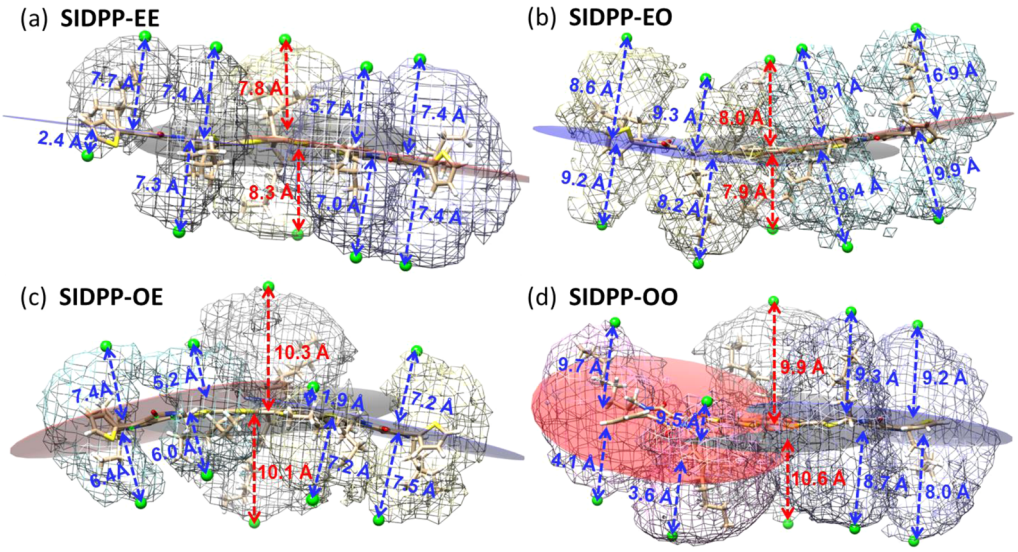

Figure 10. Top views of (a) SIDPP-EE, (b) SIDPP-EO, (c) SIDPP-OE, and (d) SIDPP-OO molecules showing the effective volumes of alkyl chains in three dimensions. The arrows indicate the farthest calculated distances that alkyl chains can extend from the molecular backbone planes.

and 61.5° for SIDPP-EE, SIDPP-EO, SIDPP-OE, and SIDPP-OO, respectively, were calculated from eq 1:

$$R = \frac{I(90) - I(0)}{I(90) + I(0)} = \frac{P(1 - 3\langle\cos^2\gamma\rangle)}{2(1 - \langle\cos^2\gamma\rangle) + P(3\langle\cos^2\gamma\rangle - 1)} \quad (1)$$

where P is the fractional polarization of the X-ray beam (0.85).[61,62] (3) The tilt angle ($\alpha = 90 - \gamma$) of the molecular backbone was then calculated to be 21.5°, 22.9°, 29.9°, and 28.5° for SIDPP-EE, SIDPP-EO, SIDPP-OE, and SIDPP-OO, respectively. The SIDPP-EE and SIDPP-EO films rendered more positive R values and lower α values, consistent with the dominantly edge-on molecular orientation indicated by GIXD. On the other hand, the SIDPP-OE and SIDPP-OO films had less positive R values, which is a result of the more disordered orientation with lower crystallinity as observed by GIXD. (It should be noted that tilt angles (or lower R values) estimated from NEXAFS data do not necessarily reflect real tile angles but may indicate averaged tilt angles of the radially oriented molecules. The SIDPP-EE and SIDPP-EO molecules are quite crystalline with long-range ordering, so that the measured tilt angles present real tilt angles. In contrast, the SIDPP-OE and SIDPP-OO molecules are much less crystalline, so that the measured tile angles present averaged tilt angles.) Therefore, NEXAFS confirmed that the SIDPP-EE and SIDPP-EO molecules displayed less tilt than SIDPP-OE and SIDPP-OO molecules while adopting edge-on orientations.

Correlation between Chemical Structure and Molecular Packing and Orientation in SIDPP Molecules. The chemical structure of the alkyl side chains has a profound effect on the molecular stacking and orientation of SIDPP molecules in annealed thin films in three ways. First, the structure of the alkyl side chains attached to the SI core significantly influences molecular packing. SIDPP-EE and SIDPP-EO molecules have much higher crystallinity and shorter $\pi-\pi$ stacking distances than SIDPP-OE and SIDPP-OO molecules. To further probe the structural cause of these differences, quantum mechanics/molecular mechanics molecular dynamics (QM/MM MD) simulations were used to determine the optimal three-dimensional (3-D) positions of the flexible alkyl side chains of the SI and DPP units. To our knowledge, the present study provides the first reported estimate of effective distance and volume occupied by flexible motions of alkyl side chains on the SIDPP backbone. The flexible motions of alkyl side chains cannot be reflected in the optimized molecular structure calculated by the DFT method. However, it can be expected that thermal energy induces the rotation of single bonds in the alkyl side chains to allow higher energy conformations even at room temperature.[63] Thus, we considered an effective distance and volume occupied by the alkyl side chains, which corresponds to the effective van der Waals volume. Figure 10 shows top views of the SIDPP molecules exhibiting alkyl side chain positions in 3-D (front views and side views are also shown in Figures S8 and S9). The arrows show the farthest distance that alkyl side chains can extend from the molecular backbone. 2-Ethylhexyl chains on the SI core occupy a smaller volume than do *n*-octyl chains. The farthest calculated distances were ~8 Å for molecules that bear 2-ethylhexyl chains on the SI core and ~10 Å for molecules that bear *n*-octyl chains on the SI core. Note that this agrees well with the optimized molecular geometries (Figure 4 and Figures S1–S3) that were calculated by the DFT method. Both molecular

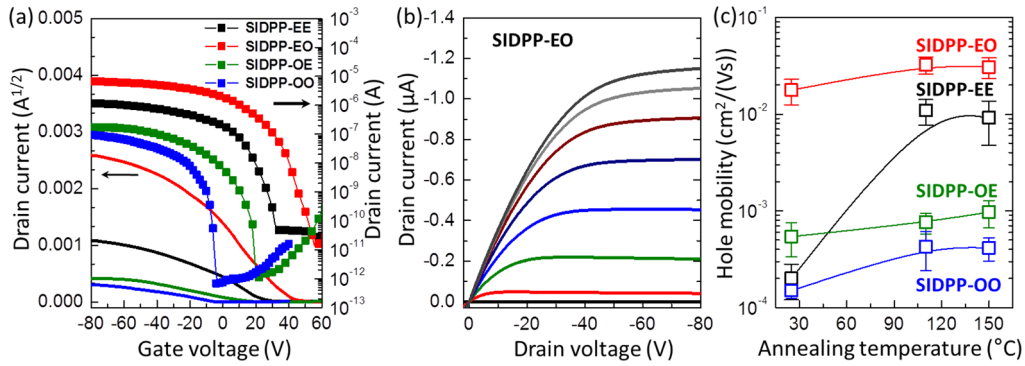

Figure 11. (a) Representative transfer characteristics at a constant $V_D = -60$ V for OFET devices based on the 110 °C-annealed SIDPP films. (b) Representative output characteristics for an OFET device based on the 110 °C-annealed SIDPP-EO film ($V_G = +60$ to -80 V, step size: -20 V). (c) Hole mobility *versus* annealing temperature plot.

geometry calculations indicate that the smaller effective volume and shorter distance of the 2-ethylhexyl groups more effectively facilitate intermolecular packing, leading to increased crystallinity and tighter molecular stacking. By contrast, longer *n*-octyl groups on the SI core prevent close molecular packing to some degree, resulting in molecular disorder within the thin film. It should also be noted that the two alkyl chains are appended at the Si atom and lie in both directions perpendicular to the molecular stacking plane, which make a greater impact on the molecular packing than does the alkyl chain on the DPP arms.

Second, the effective size of the alkyl side chains on the SI core affected the overall molecular orientation. The SIDPP molecules tended to be randomly oriented and nearly amorphous (Figure S6) immediately following spin-coating. This is because during this fast drying process there were a lack of external stimulations for molecules to self-organize, typically resulting in molecules near the substrate adopting a face-on orientation by cofacial van der Waals interactions.[64−66] Annealing allows molecules to move more freely and to pack more closely due to strong intermolecular $\pi-\pi$ interactions.[25,57,67] SIDPP-EE and SIDPP-EO molecules containing smaller 2-ethylhexyl groups on the SI core can pack more tightly, leading to predominantly edge-on orientations. Conversely, SIDPP-OE and SIDPP-OO molecules with bulkier *n*-octyl groups on the SI core are less likely to self-assemble, thereby adopting more random orientations.

This dependence of molecular orientation on the kind of substituted alkyl chains on the SI core can be explained as follows: Molecular orientation is affected by several factors including molecule−substrate interactions at the bottom of the film, molecule−molecule interactions in the bulk, molecular solubility, and the conditions under which the films were formed.[19,20,64,67] Molecular reorganization during annealing tends to yield linear flat aromatic molecules (like SIDPP-EE and SIDPP-EO) in an edge-on orientation, since the edge-on oriented molecular assembly is more thermodynamically favored.[64] On the other hand, aromatic molecules having bulky substituents (like SIDPP-OE and SIDPP-OO) tend to adopt a more face-on orientation because cofacial van der Waals interactions between the π-conjugated backbone and substrate surface prevail energetically.[19,20,67]

Third, alkyl side chains on the DPP moieties significantly influenced molecular stacking in the out-of-plane direction, as determined by comparing the out-of-plane spacings (d_L) found by X-ray diffraction and molecular widths (d_{1-2}, Figure 4 and Figures S1−S3) obtained from DFT-optimized molecular geometries for each of the SIDPP molecules. The (d_L, d_{1-2}) values were calculated to be (17.1, 18.82 Å), (19.0, 22.64 Å), (17.9, 18.45 Å), and (18.9, 24.43 Å) for SIDPP-EE, SIDPP-EO, SIDPP-OE, and SIDPP-OO, respectively. The differences between the d_L and d_{1-2} values are small for SIDPP-EE and SIDPP-OE molecules (1.72 and 0.55 Å, respectively), bearing the 2-ethylhexyl groups on the DPP side arms, but much greater for SIDPP-EO and SIDPP-OO (3.64 and 5.50 Å, respectively), bearing *n*-octyl groups. The larger ($d_{1-2} - d_L$) differences in the SIDPP-EO and SIDPP-OO films suggest that there is some degree of interdigitation between the *n*-octyl chains on the DPP side arms, causing them to preferentially lie in the out-of-plane direction. In this manner, SIDPP-EO and SIDPP-OO display increased intermolecular attraction, consistent with the observed increase in T_m. In short, 2-ethylhexyl groups on the DPP side arms induce weak interactions between molecules in the vertical direction, whereas *n*-octyl groups created interdigitations with increased intermolecular interactions. Furthermore, these molecular stackings and orientations directly influence the electrical properties of OFET and OPV devices.

OFET Properties. Bottom-gate top-contact organic field-effect transistors were employed to evaluate the electrical properties of the SIDPP films annealed at 25, 110, and 150 °C. Figure 11a shows the representative drain current (I_D) *versus* gate voltage (V_G) plots at a drain voltage (V_D) of -60 V for OFETs based on SIDPP films annealed at 110 °C. The hole mobilities of the devices were calculated in their respective saturation

TABLE 2. Electrical Parameters of the OFET Devices Based on the SIDPP Molecular Films

	as-cast film			110 °C-annealed film			150 °C-annealed film		
molecule	μ_h (cm^2/V^{-1} s^{-1})	on/off ratio	V_{on} (V)	μ_h (cm^2/V^{-1} s^{-1})	on/off ratio	V_{on} (V)	μ_h (cm^2/V^{-1} s^{-1})	on/off ratio	V_{on} (V)
SIDPP-EE	2.0×10^{-4}	2.2×10^{3}	−6	1.1×10^{-2}	2.5×10^{4}	32	0.9×10^{-2}	2.5×10^{4}	34
SIDPP-EO	1.8×10^{-2}	8.0×10^{4}	22	3.2×10^{-2}	7.1×10^{5}	56	3.1×10^{-2}	5.7×10^{4}	50
SIDPP-OE	5.4×10^{-4}	1.9×10^{4}	−4	7.6×10^{-4}	1.7×10^{5}	20	9.7×10^{-4}	7.9×10^{5}	24
SIDPP-OO	1.5×10^{-4}	1.5×10^{3}	30	4.3×10^{-4}	1.4×10^{5}	−4	4.2×10^{-4}	3.2×10^{4}	−6

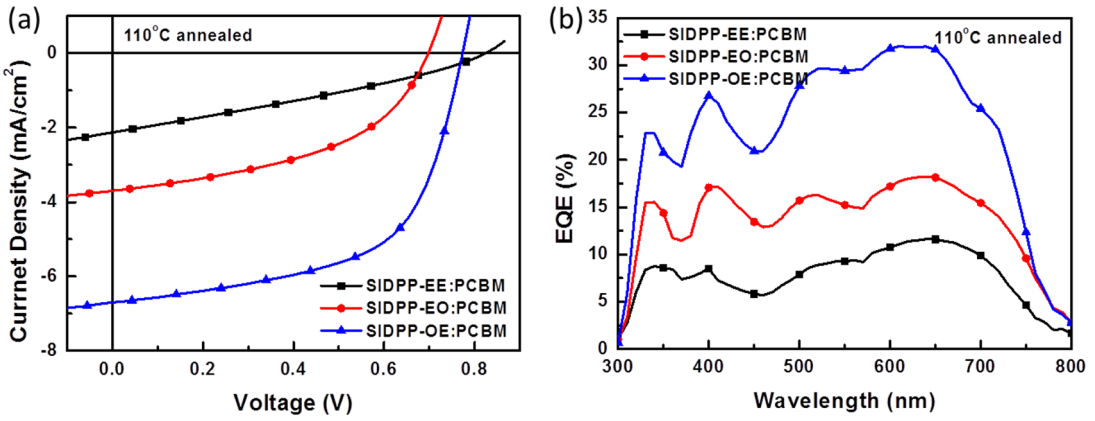

Figure 12. (a) Photocurrent density−voltage characteristics and (b) EQE spectra of the 110 °C-annealed SIDPP:PCBM (1:1, wt/wt)-based photovoltaic devices, measured under AM 1.5 G, 100 mW/cm^2. The devices were postannealed at 110 °C.

regimes according to the relationship $I_D = C_i\mu W(V_G - V_{th})^2/2L$, where W and L are the channel width (800 μm) and length (100 μm), respectively, C_i is the specific capacitance of the gate dielectric (11 nF/cm^2), V_{th} is the threshold voltage, and μ is the hole mobility. Figure 11b shows the representative output characteristics (I_D *versus* V_D) at eight different V_G's for OFETs based on SIDPP-EO, which displayed well-behaved p-type transistor characteristics, including a linear regime and a saturation regime. The hole mobilities of the OFETs based on the SIDPP films are summarized in Figure 11c and Table 2. All of the OFETs based on as-cast SIDPP films exhibited hole mobilities on the order of 10^{-4} cm^2 V^{-1} s^{-1}, except for the device based on SIDPP-EO films. This is possibly because of the lack of crystallinity and molecular orientational consistency (see Figure S6). The as-cast SIDPP-EO film showed the highest hole mobility of 1.8×10^{-2} cm^2 V^{-1} s^{-1}. The superior performance of the latter film is likely due to its highly crystalline structure even at the as-cast condition. Thermal annealing of the SIDPP films generally increased the hole mobility, with the effect depending strongly on the degree to which the crystallinity and molecular orientation were improved. A dramatic increase in hole mobility was observed in SIDPP-EE films, from 2.0×10^{-4} cm^2 V^{-1} s^{-1} to 1.1×10^{-2} cm^2 V^{-1} s^{-1} upon annealing at 110 °C. By contrast, SIDPP-OE and SIDPP-OO films exhibited moderate increases consistent with the smaller observed change in crystallinity upon annealing (Figure S6c,d and Figure 6c,d). The 110 °C-annealed SIDPP-EO films showed the highest hole mobility of 3.2×10^{-2} cm^2 V^{-1} s^{-1}, which is among the highest hole mobilities reported to date for DPP-based small molecules.[27,68−70] Overall, we demonstrate that the hole mobilities are strongly correlated with the crystallinity and molecular orientation in films.

TABLE 3. Summary of Photovoltaic Parameters and SCLC Hole Mobilities of SIDPP:PCBM Devices

material		V_{oc} (V)	J_{sc} (mA/cm^2)	FF	PCE (%)	μ_h (cm^2 V^{-1} s^{-1})
SIDPP-EE:PCBM (1:1)	as-cast	0.82	5.1	0.38	1.6	2.7×10^{-5}
	110 °C-annealed	0.82	2.1	0.30	0.5	1.1×10^{-6}
SIDPP-EO:PCBM (1:1)	as-cast	0.74	4.9	0.31	1.1	6.4×10^{-6}
	110 °C-annealed	0.70	3.7	0.47	1.2	2.8×10^{-5}
SIDPP-OE:PCBM (1:1)	as-cast	0.81	5.3	0.34	1.5	6.9×10^{-5}
	110 °C-annealed	0.77	7.5	0.60	3.5	8.7×10^{-4}

Photovoltaic Properties. OPV devices based on the SIDPPs were fabricated with the structure ITO/PEDOT:PSS/SIDPP:PCBM (1:1, wt/wt)/Al, and their photovoltaic properties were measured under AM 1.5 G, 1 sun illumination. Figure 12 shows photocurrent density (J) *versus* voltage (V) curves and external quantum efficiency (EQE) spectra of the OPV devices, and Table 3 summarizes their photovoltaic properties. The SIDPP-OO films were excluded from the OPV study because the solubility of SIDPP-OO was too low for OPV fabrication. The as-cast SIDPP-EE, SIDPP-EO, and SIDPP-OE devices exhibited similar PCEs in the range 1.1−1.6%. After annealing at 110 °C, the SIDPP-EE and

SIDPP-EO devices showed nearly the same or poorer PCEs. On the other hand, the PCEs of SIDPP-OE devices increased significantly, from 1.5% to 3.5%. This PCE increase was due mainly to a dramatic improvement in the short-circuit current density (J_{sc}), 7.5 mA cm^{-2}, and the fill factor (FF), 0.60.

To better understand the photovoltaic properties, we characterized the SIDPP:PCBM blend films. Figure 13 shows GIXD patterns of as-cast and 110 °C-annealed SIDPP:PCBM blend films. SIDPP molecular domains in the as-cast films were weakly crystalline, just as in the unblended SIDPP films. When annealed at 110 °C, the SIDPP-EE:PCBM and SIDPP-EO:PCBM films displayed increased crystallinity, indicative of phase-separated domains. The SIDPP-EE molecules, in particular, showed multiple ordered peaks in the q_{yz} plane with an increase in the feature corresponding to crystalline PCBM at around $q = 1.4$ Å^{-1}. The two (010) peaks in the in-plane (q_y) direction correspond to peaks at the same positions in the GIXD pattern of the pure SIDPP-EE film. The SIDPP-EO molecules in the blend films showed similar behavior. Average out-of-plane spacings were estimated to be $d = 16.7$ Å and $d = 18.3$ Å for the SIDPP-EE and SIDPP-EO in the blended films, respectively. These values are close to but slightly smaller than those of the 110 °C-annealed pure SIDPP-EE and SIDPP-EO films. These observations suggest that the SIDPP-EE and SIDPP-EO molecules form well-ordered edge-on oriented stacking between semicrystalline PCBM domains with slightly reduced crystallinity compared to the corresponding unblended films. By contrast, the annealed SIDPP-OE:PCBM film showed weak and slightly increased crystallinity compared to the as-cast film. The reduction in crystallinity presumably results from not only the originally weaker molecular packing but also interference by PCBM molecules. However, this suggests that the high interfacial area between the SIDPP-OE and PCBM molecules can be maintained while each nanoscopic molecular domain forms, a beneficial characteristic for high-performance OPVs.

Hole mobility in SIDPP:PCBM blend films was determined by the space-charge-limited-current (SCLC) method, where hole-only devices were fabricated with the structure ITO/PEDOT:PSS/SIDPP:PCBM (1:1, wt/wt)/Au and their current−voltage characteristics were measured in the absence of light. Table 3 summarizes the hole mobilities of the as-cast and 100 °C-annealed blend films. After annealing the blend films at 110 °C, SIDPP-EE:PCBM hole mobility decreased from 2×10^{-5} cm^2 V^{-1} s^{-1} to 1.1×10^{-6} cm^2 V^{-1} s^{-1}. The SIDPP-EO:PCBM film showed a slight increase from 6.4×10^{-6} cm^2 V^{-1} s^{-1} to 2.8×10^{-5} cm^2 V^{-1} s^{-1}. By contrast, the SIDPP-OE:PCBM film showed a large increase from 6.9×10^{-5} cm^2 V^{-1} s^{-1} to 8.7×10^{-4} cm^2 V^{-1} s^{-1}, a key factor contributing to high J_{sc} values. The trend in the hole mobility is strongly associated with the SIDPP molecular orientation and SIDPP:PCBM blend morphology in the films. GIXD (Figure 13d,e) revealed that

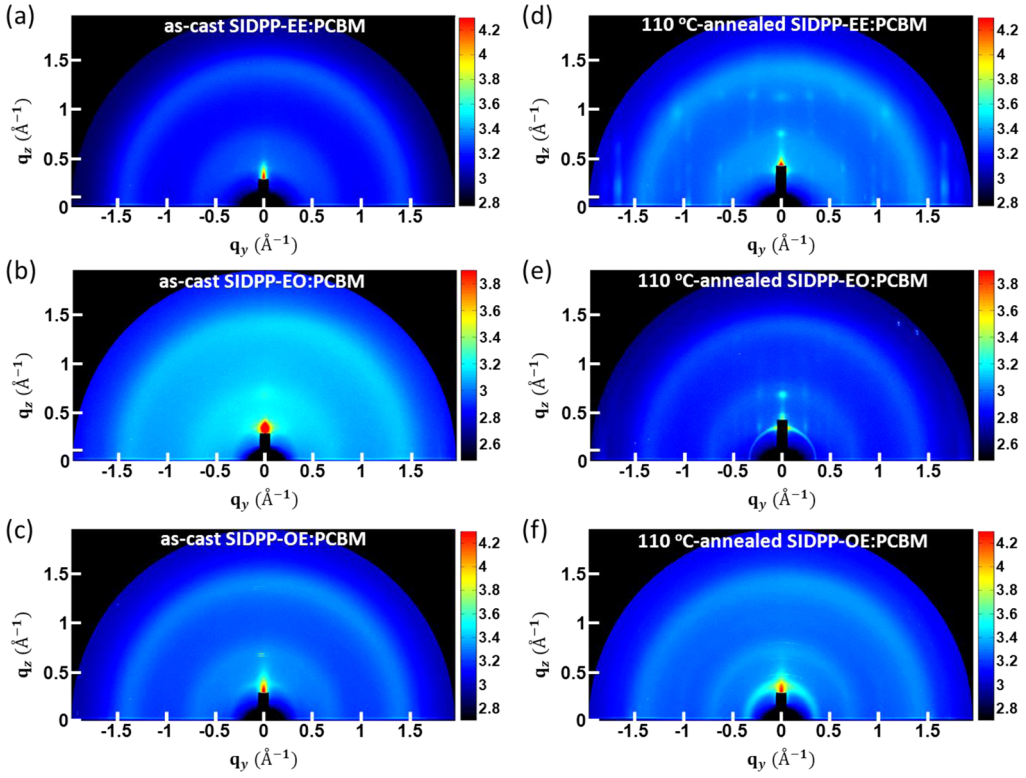

Figure 13. GIXD images of as-cast (a) SIDPP-EE:PCBM, (b) SIDPP-EO:PCBM, and (c) SIDPP-OE:PCBM blend films. GIXD images of 110 °C-annealed (d) SIDPP-EE:PCBM, (e) SIDPP-EO:PCBM, and (f) SIDPP-OE:PCBM blend films.

the SIDPP-EE and SIDPP-EO molecules assumed edge-on molecular stacking between PCBM domains such that hole mobility in the vertical direction improves minimally for SIDPP-EO:PCBM blends and declines for SIDPP-EE:PCBM blends. By contrast, SIDPP-OE molecules showed improved hole mobility in the blend by adopting a more radial molecular orientation with increased molecular stacking after thermal annealing (Figure 13f). Moreover, the continuous nanoscale connections between SIDPP-OE molecules revealed by morphology studies contributed to the efficient hole transport. (The morphological features of the SIDPP:PCBM blend films were thoroughly investigated using TEM, AFM, and UV−visible spectroscopy and discussed in the Supporting Information.) Therefore, the photovoltaic properties are strongly correlated with molecular orientation, morphology, and carrier mobility, which was effectively controlled by the mixed attachment of branched and linear alkyl chains.

CONCLUSION

To investigate the effect of substituted alkyl side chains on molecular packing, crystallinity, and orientation in SIDPP molecules, we synthesized and characterized four molecular variants bearing 2-ethylhexyl (E), *n*-octyl (O), or both E and O side groups. X-ray diffraction and NEXAFS studies revealed that the crystallinity and molecular orientation of the SIDPP molecular films strongly depended on the type of alkyl side chains in the molecules and annealing conditions. After thermal annealing, SIDPP-EE and SIDPP-EO, which contain 2-ethylhexyl groups on the SI moiety, exclusively adopted edge-on molecular orientations with high crystallinity. By contrast, SIDPP-OE and SIDPP-OO, which contain *n*-octyl substituents on the SI moiety, preferred radial orientations. This indicates that 2-ethylhexyl groups on the SI core facilitate intimate molecular packing, whereas the longer *n*-octyl groups prevent close molecular packing to some degree, resulting in greater molecular disordering in thin films. Linear *n*-octyl substituents attached to DPP side arms effectively facilitated molecular packing in the vertical direction relative to the substrates *via* octyl−octyl interdigitation. This molecular stacking directly impacts the electrical properties of the cast films. Highly edge-on oriented SIDPP-EO molecules exhibited the highest hole mobility of the synthesized SIDPP variants (3.2×10^{-2} $cm^2 V^{-1} s^{-1}$). This is one of the highest hole mobilities reported for solution-processable DPP-based small molecules. SIDPP-OE molecules adopted a radial distribution of molecular orientations in SIDPP-OE:PCBM blend films with the greatest PCE value of 3.5%. Collectively, this work clearly shows the good correlation between electrical properties and molecular packing and orientation, which was optimized by altering the alkyl side chains attached to a molecular backbone.

METHODS/EXPERIMENTAL SECTION

^{1}H NMR spectra were taken on a 400 MHz Bruker advance 400 spectrometer. Molecular weights were measured by matrix-assisted laser desorption/ionization time-of-flight mass spectrometry (MALDI-TOF MS) that was performed on a Bruker Autoflex III instrument. Differential scanning calorimetry (DSC) data were recorded on a PerkinElmer Pyris 1 DSC instrument at a heating rate of 10 °C/min between 30 and 300 °C under nitrogen. UV−visible absorption spectra were recorded on a PerkinElmer Lambda 9 UV−vis spectrophotometer. Cyclic voltammograms were performed on a CH Instruments electrochemical analyzer, and degassed acetonitrile solutions containing 0.1 M tetrabutylammonium hexafluorophosphate ($TBAPF_6$) as the electrolyte were used. The voltage scan rate was 50 mV/s. A Pt wire electrode dip-coated with a thin film of the molecule was used as the working electrode, another Pt wire was used as the counter electrode, Ag wire (Ag/Ag^+) was the reference electrode, and ferrocene (Fc) was used as the internal standard for energy calibration (Fc/Fc^+ potential was assumed to be 4.8 eV). X-ray diffraction data were recorded on a Bruker D8 Advance X-ray diffractometer using Cu Kα radiation (λ = 0.1542 nm) at room temperature. Grazing incidence X-ray diffraction patterns were taken at the 9A beamline of the Pohang Light Source (PLS) in Korea. The wavelength of X-rays was 0.1114 or 0.1101 nm, and the incidence angle was 0.13°, the angle between the critical angle of the sample and that of Si. A 2D CCD detector (model: Rayonix 2D SX165) was used. Near-edge X-ray absorption fine structure spectroscopy was performed at the 10D XAS-KIST beamline of the Pohang Light Source in the Pohang Accelerator Laboratory with 3 GeV energy and 250 mA storage ring current in top-up mode (constant current). NEXAFS measurements were conducted at ultrahigh vacuum (10^{-9} Torr) at 300 K with a beamline resolution of about 600 meV at carbon K-edge energy. Carbon K-edge collection was performed in total-electron-yield mode with a sample current measurement. Spectra collected at six incidence angles with respect to the surface plane, *i.e.*, 15°, 30°, 45°, 60°, 75°, and 90°, were normalized by subtracting the spectra at 280 eV and normalizing with respect to carbon concentration by their intensity at 330 eV. The surface morphology of the samples was investigated by tapping mode atomic force microscopy (AFM) (D3100 Nanoscope V, Veeco) and transmission electron microscopy (TEM) (PhilipsCM-30).

Simulations of the Effective Volume with Quantum Mechanics/Molecular Mechanics Molecular Dynamics Simulation). Molecular dynamics simulations were performed to measure the solvent-accessible surface of alkyl side chains attached to the SIDPP backbone. As shown in DFT-optimized structures, SIDPP has mostly planar structure due to the π-conjugation along the backbone consisting of SI and DPP units. Classical MD simulation cannot properly describe the rigidity of conjugated systems and allows rotation along the double bond with a relatively small activation energy. To overcome this, we chose the MD simulation with AM1 potential using the semiempirical quantum method based on the Hartree−Fock formalism. Even though semiempirical methods give us a good balance between computational accuracy and cost, it is still not enough to correctly consider highly conjugated systems. To improve the rotational potential along the bond between SI and the DPP unit, the potential energy surface was obtained through the scan coordinate methods implemented in Gaussian 09. Here, the dihedral angle between SI and the DPP unit was scanned with a step size of 10°. At each dihedral angle, the structure was optimized through DFT calculations using B3LYP with a valence double-ζ polarized basis set, 6-311G(d,p), and the energy was

calculated. With the resulting potential energy surface, we obtained the rotational energy barrier gap between the DFT and AM1 methods as described in Figures S13 and S14. As a result, we could describe the SIDPP backbone as if we used quantum mechanical methods with a high basis set by performing the MD simulation with AM1 methods. This approach gave us the advantage of saving time and increasing accuracy simultaneously. The MD simulation with the AM1 method was supported in the Amber 12 molecular dynamics program.

Occupancies of each different alkyl side chain on the SIDPP backbone can be represented as a three-dimensional grid of values by using UCSF Chimera. Before getting the occupancy we defined a reference set of atoms to hold steady to keep these atoms in the same place as much as possible, and then the trajectory frames were transformed. In this case, we selected three atoms on each backbone anchored to the alkyl chains. To estimate and represent the effective volume involved in the intermolecular interaction, it was necessary to offer a new parameter. Thus, we set the planes composed of backbone units and the points to the greatest point (green ball) on the volume. With this, we offered a mean effective distance as the parameter by measuring the distance from the planes to the points.

Fabrication of Organic Field-Effect Transistors. OFET devices were fabricated on a highly doped n-type Si wafer with a thermally grown 300 nm thick oxide layer. The doped n-type Si wafer served as the gate electrode, and a thermally grown 300 nm thick SiO_2 layer acted as a gate insulator. The wafer was cleaned in piranha solution for 30 min at 100 °C and washed with distilled water. Then, the SiO_2 layer was treated with octadecyltrichlorosilane (ODTS, Gelest, Inc.) to remove the hydrophilic silanol groups on SiO_2. A 40 nm thick layer of the SIDPP molecules was spin-coated from a 0.5 wt % chloroform solution onto the ODTS-treated substrates. After spin-coating, the samples were dried in a vacuum chamber for 24 h. The molecular films were thermally annealed for 30 min in a vacuum chamber at three temperatures, RT (as-cast), 110 °C, and 150 °C. The 50 nm thick Au was vacuum-deposited through a shadow mask on the molecular film to form source/drain electrodes with channel lengths and widths of 50 and 800 μm, respectively. Current−voltage characteristics of the resulting OFET devices were measured using Keithley 2400 and 236 source/measure units under vacuum conditions (10^{-5} Torr) in a dark environment at room temperature.

Fabrication of Hole-Only Devices. Hole mobilities were measured on hole-only devices with a structure of ITO/PEDOT:PSS/SIDPP:PCBM (1:1 wt/wt) blend film/Au. Current density *versus* voltage characteristics were recorded under dark on a Keithley model 2400 source measuring unit. Hole mobilities were determined using the SCLC method, based on the following equation:

$$J = \frac{9}{8}\varepsilon_r\varepsilon_o\mu_h\frac{V^2}{L^3} \quad (1)$$

where ε_o is the permittivity of free space, ε_r is the dielectric constant of the blend film (assumed to be 3), μ_h is the hole mobility, $V = V_{appl} - V_{bi} - V_a$ (V_{appl}, the applied bias; V_{bi}, the built-in potential due to the difference in electrical contact work function; V_a, the voltage drop due to contact resistance and series resistance across the electrodes), and L is the thickness of a photoactive layer.

Fabrication of Organic Solar Cells. OPV cells were fabricated using a photoactive layer of SIDPP (SIDPP-EE, SIDPP-EO, SIDPP-OE, or SIDPP-OO):PCBM blend film. Prior to device fabrication, the ITO-coated glass substrates (15 Ω/sq, 2.5 × 2.5 cm^2) were cleaned ultrasonically in isopropyl alcohol, acetone, and isopropyl alcohol, for 10 min each. The ITO glass substrates were then treated with UV/O_3 for 15 min. The clean ITO substrate was coated with a 30 nm thick layer of poly(3,4-ethylenedioxythiophene):poly(styrenesulfonate) (PEDOT:PSS) at 80 °C for 10 min. On top of the PEDOT:PSS layer photoactive layers were formed by spin-coating using a chloroform solution (12 mg/mL) containing an SIDPP molecule and PCBMs at various ratios of 7:3, 1:2, 1:1, and 3:7 (w/w). The thickness of the photoactive layer was ~90 nm. Lastly, a 100 nm thick Al layer was thermally evaporated through a shadow mask at a pressure of less than 2×10^{-6} Torr with a deposition rate of ~5 Å/s. The active area was 0.12 cm^2. After the Al deposition, OPV devices were annealed at 80, 110, and 150 °C for 10 min. The 1:1 (w/w) ratio and 110 °C thermal annealing were optimal for photovoltaic performance. Photocurrent density *versus* voltage (*J*−*V*) characteristics were recorded on a Keithley model 2400 source measuring unit. A class-A solar simulator with a 1000 W xenon lamp (Yamashita Denso) equipped with a KG-5 filter was used to measure photovoltaic performance. Its light intensity was adjusted to 100 mW/cm^2 with AM 1.5 G 1 sun light using an NREL-calibrated mono Si solar cell. EQE spectra were taken as a function of wavelength from 300 to 800 nm on an incident photon-to-current conversion equipment (PV Measurement Inc.). Calibration was performed using a G425 silicon photodiode, which is NIST-calibrated as a standard.

Conflict of Interest: The authors declare no competing financial interest.

Acknowledgment. This work was supported by New and Renewable Energy Program of the Korea Institute of Energy Technology Evaluation and Planning (KETEP) grant funded by the Korea Goverment Ministry of Trade, Industry & Energy (MTIE) (20133030000130, 20113030010060), and by Korea Research Council of Fundamental Science and Technology (KRCF) and Korea Institute of Science and Technology (KIST) for "NAP National Agenda Project Program" and Project No. 2E24821, and by the National Research Foundation of Korea Grant funded by the Korean Government (MSIP) (2013, University-Institute corporation program).

Supporting Information Available: Synthesis of SIDPP molecules; morphological features and discussion of the SIDPP:PCBM blend films. This material is available free of charge *via* the Internet at http://pubs.acs.org.

REFERENCES AND NOTES

1. Nielsen, C. B.; Turbiez, M.; McCulloch, I. Recent Advances in the Development of Semiconducting DPP-Containing Polymers for Transistor Applications. *Adv. Mater.* **2012**, *25*, 1859–1880.
2. Mei, J.; Diao, Y.; Appleton, A. L.; Fang, L.; Bao, Z. Integrated Materials Design of Organic Semiconductors for Field-Effect Transistors. *J. Am. Chem. Soc.* **2013**, *135*, 6724–6746.
3. Li, G.; Shrotriya, V.; Huang, J.; Yao, Y.; Moriarty, T.; Emery, K.; Yang, Y. High-Efficiency Solution Processable Polymer Photovoltaic Cells by Self-Organization of Polymer Blends. *Nat. Mater.* **2005**, *4*, 864–868.
4. Ma, W.; Yang, C.; Gong, X.; Lee, K.; Heeger, A. J. Thermally Stable, Efficient Polymer Solar Cells with Nanoscale Control of the Interpenetrating Network Morphology. *Adv. Funct. Mater.* **2005**, *15*, 1617–1622.
5. He, Z.; Zhong, C.; Su, S.; Xu, M.; Wu, H.; Cao, Y. Enhanced Power−Conversion Efficiency in Polymer Solar Cells Using an Inverted Device Structure. *Nat. Photonics* **2012**, *6*, 593–597.
6. Sirringhaus, H.; Brown, P. J.; Friend, R. H.; Nielsen, M. M.; Bechgaard, K.; Langeveld-Voss, B. M. W.; Spiering, A. J. H.; Janssen, R. A. J.; Meijer, E. W.; Herwig, P.; de Leeuw, D. M. Two-Dimensional Charge Transport in Self-Organized, High-Mobility Conjugated Polymers. *Nature* **1999**, *401*, 685–688.
7. Kim, Y.; Cook, S.; Tuladhar, S. M.; Choulis, S. A.; Nelson, J.; Durrant, J. R.; Bradley, D. D. C.; Giles, M.; McCulloch, I.; Ha, C.-S.; *et al.* Strong Regioregularity Effect in Self-Organizing Conjugated Polymer Films and High-Efficiency Polythiophene:Fullerene Solar Cells. *Nat. Mater.* **2006**, *5*, 197–203.
8. Street, R. A.; Northrup, J. E.; Salleo, A. Transport in Polycrystalline Polymer Thin-Film Transistors. *Phys. Rev. B* **2005**, *71*, 165202.
9. Zaumseil, J.; Sirringhaus, H. Electron and Ambipolar Transport in Organic Field-Effect Transistors. *Chem. Rev.* **2007**, *107*, 1296–1323.
10. Facchetti, A. π-Conjugated Polymers for Organic Electronics and Photovoltaic Cell Applications. *Chem. Mater.* **2010**, *23*, 733–758.

11. Newman, C. R.; Frisbie, C. D.; da Silva Filho, D. A.; Brédas, J.-L.; Ewbank, P. C.; Mann, K. R. Introduction to Organic Thin Film Transistors and Design of N-Channel Organic Semiconductors. *Chem. Mater.* **2004**, *16*, 4436–4451.
12. Li, G.; Zhu, R.; Yang, Y. Polymer Solar Cells. *Nat. Photonics* **2012**, *6*, 153–161.
13. Beaujuge, P. M.; Fréchet, J. M. Molecular Design and Ordering Effects in π-Functional Materials for Transistor and Solar Cell Applications. *J. Am. Chem. Soc.* **2011**, *133*, 20009–20029.
14. Thompson, B. C.; Fréchet, J. M. J. Polymer–Fullerene Composite Solar Cells. *Angew. Chem., Int. Ed.* **2008**, *47*, 58–77.
15. Coughlin, J. E.; Henson, Z. B.; Welch, G. C.; Bazan, G. C. Design and Synthesis of Molecular Donors for Solution-Processed High-Efficiency Organic Solar Cells. *Acc. Chem. Res.* **2013**, *47*, 257–270.
16. Liu, Y.; Wan, X.; Wang, F.; Zhou, J.; Long, G.; Tian, J.; Chen, Y. High-Performance Solar Cells using a Solution-Processed Small Molecule Containing Benzodithiophene Unit. *Adv. Mater.* **2011**, *23*, 5387–5391.
17. Guo, X.; Zhou, N.; Lou, S. J.; Hennek, J. W.; Ponce Ortiz, R. o.; Butler, M. R.; Boudreault, P.-L. T.; Strzalka, J.; Morin, P.-O.; Leclerc, M. Bithiopheneimide-Dithienosilole/Dithienogermole Copolymers for Efficient Solar Cells: Information from Structure–Property–Device Performance Correlations and Comparison to Thieno[3,4-*c*]pyrrole-4,6-dione Analogues. *J. Am. Chem. Soc.* **2012**, *134*, 18427–18439.
18. Liu, F.; Gu, Y.; Jung, J. W.; Jo, W. H.; Russell, T. P. On the Morphology of Polymer-Based Photovoltaics. *J. Polym. Sci., Part B: Polym. Phys.* **2012**, *50*, 1018–1044.
19. Chen, M. S.; Niskala, J. R.; Unruh, D. A.; Chu, C. K.; Lee, O. P.; Fréchet, J. M. J. Control of Polymer-Packing Orientation in Thin Films through Synthetic Tailoring of Backbone Coplanarity. *Chem. Mater.* **2013**, *25*, 4088–4096.
20. Yokoyama, D.; Setoguchi, Y.; Sakaguchi, A.; Suzuki, M.; Adachi, C. Orientation Control of Linear–Shaped Molecules in Vacuum-Deposited Organic Amorphous Films and Its Effect on Carrier Mobilities. *Adv. Funct. Mater.* **2010**, *20*, 386–391.
21. Chen, Y.; Wan, X.; Long, G. High Performance Photovoltaic Applications Using Solution-Processed Small Molecules. *Acc. Chem. Res.* **2013**, *46*, 2645–2655.
22. Kyaw, A. K. K.; Wang, D. H.; Wynands, D.; Zhang, J.; Nguyen, T.-Q.; Bazan, G. C.; Heeger, A. J. Improved Light Harvesting and Improved Efficiency by Insertion of an Optical Spacer (ZnO) in Solution-Processed Small-Molecule Solar Cells. *Nano Lett.* **2013**, *13*, 3796–3801.
23. Walker, B.; Tamayo, A. B.; Dang, X. D.; Zalar, P.; Seo, J. H.; Garcia, A.; Tantiwiwat, M.; Nguyen, T. Q. Nanoscale Phase Separation and High Photovoltaic Efficiency in Solution-Processed, Small-Molecule Bulk Heterojunction Solar Cells. *Adv. Funct. Mater.* **2009**, *19*, 3063–3069.
24. Lin, Y.; Ma, L.; Li, Y.; Liu, Y.; Zhu, D.; Zhan, X. A Solution-Processable Small Molecule Based on Benzodithiophene and Diketopyrrolopyrrole for High-Performance Organic Solar Cells. *Adv. Energy Mater.* **2013**, *3*, 1166–1170.
25. Eisenmenger, N. D.; Su, G. M.; Welch, G. C.; Takacs, C. J.; Bazan, G. C.; Kramer, E. J.; Chabinyc, M. L. Effect of Bridging Atom Identity on the Morphological Behavior of Solution–Processed Small Molecule Bulk Heterojunction Photovoltaics. *Chem. Mater.* **2013**, *25*, 1688–1698.
26. Walker, B.; Liu, J.; Kim, C.; Welch, G. C.; Park, J. K.; Lin, J.; Zalar, P.; Proctor, C. M.; Seo, J. H.; Bazan, G. C.; *et al.* Optimization of Energy Levels by Molecular Design: Evaluation of Bis-Diketopyrrolopyrrole Molecular Donor Materials for Bulk Heterojunction Solar Cells. *Energy Environ. Sci.* **2013**, *6*, 952–962.
27. Loser, S.; Bruns, C. J.; Miyauchi, H.; Ortiz, R. P.; Facchetti, A.; Stupp, S. I.; Marks, T. J. A Naphthodithiophene–Diketopyrrolopyrrole Donor Molecule for Efficient Solution-Processed Solar Cells. *J. Am. Chem. Soc.* **2011**, *133*, 8142–8145.
28. Sun, Y.; Welch, G. C.; Leong, W. L.; Takacs, C. J.; Bazan, G. C.; Heeger, A. J. Solution-Processed Small-Molecule Solar Cells with 6.7% Efficiency. *Nat. Mater.* **2011**, *11*, 44–48.
29. Zhou, J.; Wan, X.; Liu, Y.; Long, G.; Wang, F.; Li, Z.; Zuo, Y.; Li, C.; Chen, Y. A Planar Small Molecule with Dithienosilole Core for High Efficiency Solution-Processed Organic Photovoltaic Cells. *Chem. Mater.* **2011**, *23*, 4666–4668.
30. Yamaguchi, S.; Tamao, K. Silole-Containing σ- and π-Conjugated Compounds. *J. Chem. Soc., Dalton Trans.* **1998**, 3693–3702.
31. Zhong, H.; Li, Z.; Deledalle, F.; Fregoso, E. C.; Shahid, M.; Fei, Z.; Nielsen, C. B.; Yaacobi-Gross, N.; Rossbauer, S.; Anthopoulos, T. D. Fused Dithienogermolodithiophene Low Band Gap Polymers for High-Performance Organic Solar Cells without Processing Additives. *J. Am. Chem. Soc.* **2013**, *135*, 2040–2043.
32. Amb, C. M.; Chen, S.; Graham, K. R.; Subbiah, J.; Small, C. E.; So, F.; Reynolds, J. R. Dithienogermole as a Fused Electron Donor in Bulk Heterojunction Solar Cells. *J. Am. Chem. Soc.* **2011**, *133*, 10062–10065.
33. Chen, H. Y.; Hou, J.; Hayden, A. E.; Yang, H.; Houk, K.; Yang, Y. Silicon Atom Substitution Enhances Interchain Packing in a Thiophene-Based Polymer System. *Adv. Mater.* **2010**, *22*, 371–375.
34. Hendriks, K. H.; Heintges, G. H. L.; Gevaerts, V. S.; Wienk, M. M.; Janssen, R. A. J. High-Molecular-Weight Regular Alternating Diketopyrrolopyrrole-Based Terpolymers for Efficient Organic Solar Cells. *Angew. Chem., Int. Ed.* **2013**, *52*, 8341–8344.
35. Meager, I.; Ashraf, R. S.; Mollinger, S.; Schroeder, B. C.; Bronstein, H.; Beatrup, D.; Vezie, M. S.; Kirchartz, T.; Salleo, A.; Nelson, J.; *et al.* Photocurrent Enhancement from Diketopyrrolopyrrole Polymer Solar Cells through Alkyl-Chain Branching Point Manipulation. *J. Am. Chem. Soc.* **2013**, *135*, 11537–11540.
36. Loser, S.; Miyauchi, H.; Hennek, J. W.; Smith, J.; Huang, C.; Facchetti, A.; Marks, T. J. A "Zig-Zag" Naphthodithiophene Core for Increased Efficiency in Solution-Processed Small Molecule Solar Cells. *Chem. Commun.* **2012**, *48*, 8511–8513.
37. Zhang, Y.; Zou, J.; Yip, H.-L.; Sun, Y.; Davies, J. A.; Chen, K.-S.; Acton, O.; Jen, A. K.-Y. Conjugated Polymers Based on C, Si and N-Bridged Dithiophene and Thienopyrroledione Units: Synthesis, Field-Effect Transistors and Bulk Heterojunction Polymer Solar Cells. *J. Mater. Chem.* **2011**, *21*, 3895–3902.
38. Carsten, B.; He, F.; Son, H. J.; Xu, T.; Yu, L. Stille Polycondensation for Synthesis of Functional Materials. *Chem. Rev.* **2011**, *111*, 1493–1528.
39. Kim, C.; Liu, J.; Lin, J.; Tamayo, A. B.; Walker, B.; Wu, G.; Nguyen, T.-Q. Influence of Structural Variation on the Solid-State Properties of Diketopyrrolopyrrole-Based Oligophenylenethiophenes: Single-Crystal Structures, Thermal Properties, Optical Bandgaps, Energy Levels, Film Morphology, and Hole Mobility. *Chem. Mater.* **2012**, *24*, 1699–1709.
40. Tamayo, A. B.; Tantiwiwat, M.; Walker, B.; Nguyen, T.-Q. Design, Synthesis, and Self-Assembly of Oligothiophene Derivatives with a Diketopyrrolopyrrole Core. *J. Phys. Chem. C* **2008**, *112*, 15543–15552.
41. Szarko, J. M.; Guo, J.; Liang, Y.; Lee, B.; Rolczynski, B. S.; Strzalka, J.; Xu, T.; Loser, S.; Marks, T. J.; Yu, L. When Function Follows Form: Effects of Donor Copolymer Side Chains on Film Morphology and BHJ Solar Cell Performance. *Adv. Mater.* **2010**, *22*, 5468–5472.
42. Usta, H.; Risko, C.; Wang, Z.; Huang, H.; Deliomeroglu, M. K.; Zhukhovitskiy, A.; Facchetti, A.; Marks, T. J. Design, Synthesis, and Characterization of Ladder-Type Molecules and Polymers. Air-Stable, Solution-Processable N–Channel and Ambipolar Semiconductors for Thin-Film Transistors *via* Experiment and Theory. *J. Am. Chem. Soc.* **2009**, *131*, 5586–5608.
43. Saiter, A.; Delpouve, N.; Dargent, E.; Saiter, J. M. Cooperative Rearranging Region Size Determination by Temperature Modulated DSC in Semi-Crystalline Poly(l-lactide acid). *Eur. Polym. J.* **2007**, *43*, 4675–4682.
44. Kim, S.-O.; An, T. K.; Chen, J.; Kang, I.; Kang, S. H.; Chung, D. S.; Park, C. E.; Kim, Y.-H.; Kwon, S.-K. H-Aggregation

Strategy in the Design of Molecular Semiconductors for Highly Reliable Organic Thin Film Transistors. *Adv. Funct. Mater.* **2011**, *21*, 1616–1623.
45. Shin, J.; Kang, N. S.; Kim, K. H.; Lee, T. W.; Jin, J.-I.; Kim, M.; Lee, K.; Ju, B. K.; Hong, J.-M.; Choi, D. H. J-Aggregation Induced Low Bandgap Anthracene-Based Conjugated Molecule for Solution-Processed Solar Cells. *Chem. Commun.* **2012**, *48*, 8490–8492.
46. Spano, F. C. The Spectral Signatures of Frenkel Polarons in H- and J-Aggregates. *Acc. Chem. Res.* **2009**, *43*, 429–439.
47. Menzel, H.; Weichart, B.; Schmidt, A.; Paul, S.; Knoll, W.; Stumpe, J.; Fischer, T. Small-Angle X-Ray Scattering and Ultraviolet–Visible Spectroscopy Studies on the Structure and Structural Changes in Langmuir–Blodgett Films of Polyglutamates with Azobenzene Moieties Tethered by Alkyl Spacers of Different Length. *Langmuir* **1994**, *10*, 1926–1933.
48. Eisfeld, A.; Briggs, J. The J- and H-Bands of Organic Dye Aggregates. *Chem. Phys.* **2006**, *324*, 376–384.
49. Clark, J.; Chang, J.-F.; Spano, F. C.; Friend, R. H.; Silva, C. Determining Exciton Bandwidth and Film Microstructure in Polythiophene Films Using Linear Absorption Spectroscopy. *Appl. Phys. Lett.* **2009**, *94*, 163306.
50. Viterisi, A.; Gispert-Guirado, F.; Ryan, J. W.; Palomares, E. Formation of Highly Crystalline and Texturized Donor Domains in $DPP(TBFu)_2$:$PC_{71}BM$ SM-BHJ Devices *via* Solvent Vapour Annealing: Implications for Device Function. *J. Mater. Chem.* **2012**, *22*, 15175–15182.
51. Shin, W.; Yasuda, T.; Watanabe, G.; Yang, Y. S.; Adachi, C. Self-Organizing Mesomorphic Diketopyrrolopyrrole Derivatives for Efficient Solution-Processed Organic Solar Cells. *Chem. Mater.* **2013**, *25*, 2549–2556.
52. Park, J. H.; Jung, E. H.; Jung, J. W.; Jo, W. H. A Fluorinated Phenylene Unit as a Building Block for High-Performance N-Type Semiconducting Polymer. *Adv. Mater.* **2013**, *18*, 2583–2588.
53. Lovinger, A. J.; Katz, H. E.; Dodabalapur, A. Direct Imaging of Conducting and Insulating Submolecularly Wide Pathways in an Organic Semiconductor. *Chem. Mater.* **1998**, *10*, 3275–3277.
54. Takacs, C. J.; Sun, Y.; Welch, G. C.; Perez, L. A.; Liu, X.; Wen, W.; Bazan, G. C.; Heeger, A. J. Solar Cell Efficiency, Self-Assembly, and Dipole–Dipole Interactions of Isomorphic Narrow-Band-Gap Molecules. *J. Am. Chem. Soc.* **2012**, *134*, 16597–16606.
55. Zhang, X.; Richter, L. J.; DeLongchamp, D. M.; Kline, R. J.; Hammond, M. R.; McCulloch, I.; Heeney, M.; Ashraf, R. S.; Smith, J. N.; Anthopoulos, T. D.; *et al.* Molecular Packing of High-Mobility Diketo Pyrrolo-Pyrrole Polymer Semiconductors with Branched Alkyl Side Chains. *J. Am. Chem. Soc.* **2011**, *133*, 15073–15084.
56. Rivnay, J.; Mannsfeld, S. C. B.; Miller, C. E.; Salleo, A.; Toney, M. F. Quantitative Determination of Organic Semiconductor Microstructure from the Molecular to Device Scale. *Chem. Rev.* **2012**, *112*, 5488–5519.
57. Liu, X.; Sun, Y.; Perez, L. A.; Wen, W.; Toney, M. F.; Heeger, A. J.; Bazan, G. C. Narrow-Band-Gap Conjugated Chromophores with Extended Molecular Lengths. *J. Am. Chem. Soc.* **2012**, *134*, 20609–20612.
58. Gevaerts, V. S.; Herzig, E. M.; Kirkus, M.; Hendriks, K. H.; Wienk, M. M.; Perlich, J.; Müller-Buschbaum, P.; Janssen, R. A. J. Influence of the Position of the Side Chain on Crystallization and Solar Cell Performance of DPP-Based Small Molecules. *Chem. Mater.* **2013**, *26*, 916–926.
59. Hähner, G. Near Edge X-Ray Absorption Fine Structure Spectroscopy as a Tool to Probe Electronic and Structural Properties of Thin Organic Films and Liquids. *Chem. Soc. Rev.* **2006**, *35*, 1244–1255.
60. DeLongchamp, D. M.; Vogel, B. M.; Jung, Y.; Gurau, M. C.; Richter, C. A.; Kirillov, O. A.; Obrzut, J.; Fischer, D. A.; Sambasivan, S.; Richter, L. J. Variations in Semiconducting Polymer Microstructure and Hole Mobility with Spin-Coating Speed. *Chem. Mater.* **2005**, *17*, 5610–5612.
61. Gurau, M. C.; Delongchamp, D. M.; Vogel, B. M.; Lin, E. K.; Fischer, D. A.; Sambasivan, S.; Richter, L. J. Measuring Molecular Order in Poly(3-alkylthiophene) Thin Films with Polarizing Spectroscopies. *Langmuir* **2007**, *23*, 834–842.
62. DeLongchamp, D. M.; Kline, R. J.; Lin, E. K.; Fischer, D. A.; Richter, L. J.; Lucas, L. A.; Heeney, M.; McCulloch, I.; Northrup, J. E. High Carrier Mobility Polythiophene Thin Films: Structure Determination by Experiment and Theory. *Adv. Mater.* **2007**, *19*, 833–837.
63. Zheng, J.; Kwak, K.; Xie, J.; Fayer, M. D. Ultrafast Carbon–Carbon Single-Bond Rotational Isomerization in Room-Temperature Solution. *Science* **2006**, *313*, 1951–1955.
64. Xu, L.; Yang, L.; Lei, S. Self-Assembly of Conjugated Oligomers and Polymers at the Interface: Structure and Properties. *Nanoscale* **2012**, *4*, 4399–4415.
65. Elemans, J. A. A. W.; Lensen, M. C.; Gerritsen, J. W.; van Kempen, H.; Speller, S.; Nolte, R. J. M.; Rowan, A. E. Scanning Probe Studies of Porphyrin Assemblies and Their Supramolecular Manipulation at a Solid–Liquid Interface. *Adv. Mater.* **2003**, *15*, 2070–2073.
66. France, C. B.; Schroeder, P. G.; Parkinson, B. A. Direct Observation of a Widely Spaced Periodic Row Structure at the Pentacene/Au(111) Interface Using Scanning Tunneling Microscopy. *Nano Lett.* **2002**, *2*, 693–696.
67. Yokoyama, D.; Sakaguchi, A.; Suzuki, M.; Adachi, C. Horizontal Orientation of Linear-Shaped Organic Molecules Having Bulky Substituents in Neat and Doped Vacuum-Deposited Amorphous Films. *Org. Electron.* **2009**, *10*, 127–137.
68. Sonar, P.; Williams, E. L.; Singh, S. P.; Manzhos, S.; Dodabalapur, A. A Benzothiadiazole End Capped Donor–Acceptor Based Small Molecule for Organic Electronics. *Phys. Chem. Chem. Phys.* **2013**, *15*, 17064–17069.
69. Tantiwiwat, M.; Tamayo, A.; Luu, N.; Dang, X.-D.; Nguyen, T.-Q. Oligothiophene Derivatives Functionalized with a Diketopyrrolopyrrolo Core for Solution-Processed Field Effect Transistors: Effect of Alkyl Substituents and Thermal Annealing. *J. Phys. Chem. C* **2008**, *112*, 17402–17407.
70. Zhang, Y.; Kim, C.; Lin, J.; Nguyen, T. Q. Solution-Processed Ambipolar Field-Effect Transistor Based on Diketopyrrolopyrrole Functionalized with Benzothiadiazole. *Adv. Funct. Mater.* **2012**, *22*, 97–105.